Optics Communications 421 (2018) 56–65

Contents lists available at ScienceDirect

Optics Communications

journal homepage: www.elsevier.com/locate/optcom

Optimization and calibration of a snapshot medium-wave infrared full-polarization-imaging system

Hongliang Wang [a,b], Jingqiu Liang [a,*]

[a] State Key Laboratory of Applied Optics, Changchun Institute of Optics, Fine Mechanics and Physics, Chinese Academy of Sciences, Changchun 130033, China
[b] University of Chinese Academy of Sciences, Beijing 100049, China

ARTICLE INFO

Keywords:
Polarization imaging
Optimization
Calibration

ABSTRACT

In order to acquire the spatial polarization information in real time, a snapshot, mid-wave infrared, full-polarization-imaging system (SMWIFPIS) is proposed in this paper. Equal weight variance was used to optimize the polarization axis direction of the linear polarizer and the fast-axis azimuth angle of the wave plate in each channel to reduce the impact of the random intensity fluctuations in the infrared detector. A calibration method of the SMWIFPIS is proposed by investigating Fourier analysis method of a rotatable retarder fixed polarizer Stokes polarimeter (RRFPSP), which is used to improve the accuracy of polarization measurement. The calibration theory of the system is deduced. Finally, the correctness of the calibration method and the performance of the SMWIFPIS are proved by experiments. The experimental results show that the measurement accuracy of the SMWIFPIS is improved obviously through error calibration and compensation, which indicates that the effectiveness of the method is validated. The information measured by the SMWIFPIS is accurate.

1. Introduction

Polarization-imaging systems can not only measure the intensity information of a target scene, but also its orientation information. Compared with traditional photometric and radiological detection techniques, the obtained information is greatly increased, which provides strong evidence for the accurate identification of the target. Therefore, they are widely used in biomedicine [1,2], remote sensing [3–7], target detection and recognition [8,9], among other fields.

In the practical application of polarization imaging technology, the instrument platform and detection target are all in motion, so the real-time detection is very important for accurate measurement of polarization information. Therefore, the real-time polarization imaging technology have been extensively studied [10–18]. However, there are three main errors to influence polarization-measurement accuracy: (1) the azimuthal angle error of the linear polarizer, which is away from the correct angular orientation, (2) the fast-axis angle error and the phase delay error of the retarder, and (3) the random fluctuation of the detector intensity. Therefore, it is necessary to optimize the system, error calibration and compensation to improve its measurement accuracy.

Currently, curve fitting [19] and equator poles [20] are the usual calibration methods of Stokes polarization imaging system. It is necessary to use the polarization state generator to produce a variety of linear independent reference light, and need to be measured at least 4 times for each reference polarization. The calibration process is complex.

To achieve real-time polarization detection in the mid-wave infrared band, we present a snapshot mid-wave infrared full-polarization-imaging system. The system polarization measurement matrix is optimized by using equal weight variance so as to improve the system performance. A calibration method of the SMWIFPIS is proposed based on Fourier analysis method of a rotatable retarder fixed polarizer Stokes polarimeter. The calibration theory of the system is deduced.

2. Polarization measurement model and optimization

2.1. Working principle

The SMWIFPIS is shown in Fig. 1. It consists of a polarization measuring structure (PMS), a microlens array, a relay imaging system, and a cooled infrared array detector. The polarization measurement structure is composed of a linear polarization array with different polarization axis directions and a quarter wave plate. The working band range of the SMWIFPIS is 3–5 μm, with a design wavelength of 4 μm.

The working principle: The light emitted by the target object at infinity incidents into the PMS that polarization modulation is performed

* Corresponding author.
E-mail address: liangjq@ciomp.ac.cn (J. Liang).

https://doi.org/10.1016/j.optcom.2018.03.063
Received 4 February 2018; Received in revised form 15 March 2018; Accepted 25 March 2018
Available online 9 April 2018

$$M_R = \begin{bmatrix} 1 & 0 & 0 & 0 \\ 0 & \cos^2 2\theta_r + \sin^2 2\theta_r \cos\delta & \sin 2\theta_r \cos 2\theta_r (1-\cos\delta) & -\sin 2\theta_r \sin\delta \\ 0 & \sin 2\theta_r \cos 2\theta_r (1-\cos\delta) & \sin^2 2\theta_r + \cos^2 2\theta_r \cos\delta & \cos 2\theta_r \sin\delta \\ 0 & \sin 2\theta_r \sin\delta & -\cos 2\theta_r \sin\delta & \cos\delta \end{bmatrix} \quad (3)$$

where θ_r is the angle of the fast axis of the quarter-wave plate relative to the x-axis and δ is the phase delay.

Box I.

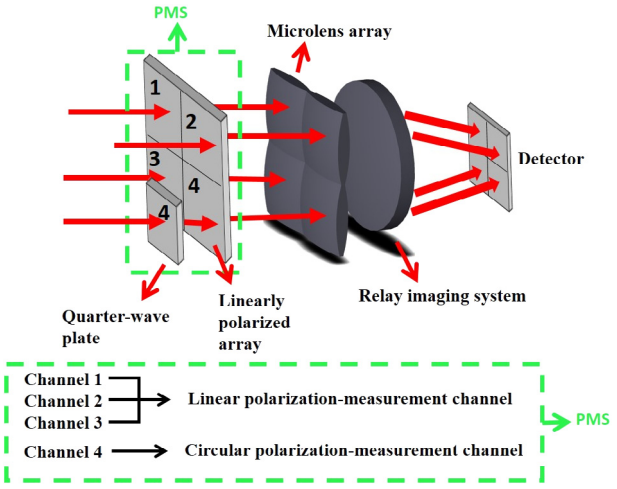

Fig. 1. Schematic layout of the SMWIFPIS.

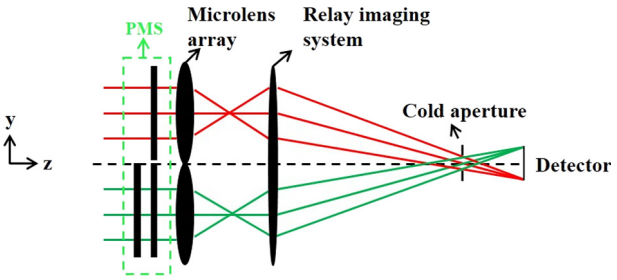

Fig. 2. The two-dimensional structure schematic diagram of the SMWIFPIS.

in the four channels, and then four images are obtained on the image plane of the microlens array. The images made by the microlens array are imaged on the target surface of the detector through a relay imaging system, and finally four intensity images are obtained respectively in the four sections of the target surface of the detector.

The infrared optical system responds to a heat source. To avoid stray light external to the scene entering the optical system and affecting the imaging, 100% cold-aperture matching should be achieved. The cold diaphragm of the cooled infrared array detector is used as the aperture stop for the SMWIFPIS. Thus, the SMWIFPIS uses a secondary imaging design method, which is shown in Fig. 2. The microlens array is used to obtain multiple images of a target. The relay imaging system is used to image the first images made by the microlens array on the detector, meanwhile it uses the cold diaphragm of the detector as its aperture stop to achieve 100% cold-aperture matching.

2.2. Polarization measurement model

When light is incident on the SMWIFPIS, the Mueller matrix in the channels 1, 2, and 3 can be expressed as:

$$M_{LP} = \frac{1}{2}\begin{bmatrix} 1 & \cos 2\theta & \sin 2\theta & 0 \\ \cos 2\theta & \cos^2 2\theta & \sin 2\theta \cos 2\theta & 0 \\ \sin 2\theta & \sin 2\theta \cos 2\theta & \sin^2 2\theta & 0 \\ 0 & 0 & 0 & 0 \end{bmatrix} \quad (1)$$

where θ is the angle between the polarizer axis of the polarizer and the x-axis.

The Mueller matrix in channel 4 can be expressed as:

$$M_4 = M_{LP} \cdot M_R \quad (2)$$

M_R can be expressed as given in Box I.

Because the Stokes vector can describe the polarization state of any light and the Muller matrix can describe all types of optical systems [21,22]. Then when the incident light passes through different polarization measurement channels of the SMWIFPIS, the relationship between the Stokes vector of the outgoing and incident light, S_{out} and S_{in}, respectively, can be obtained as:

$$S_{out} = \begin{cases} M_{LP}(\theta_{pi}) \cdot S_{in}(S_0, S_1, S_2, S_3) & i = 1,2,3 \\ M_4 \cdot S_{in}(S_0, S_1, S_2, S_3) & i = 4 \end{cases} \quad (4)$$

Currently, the detector can only respond to the light intensity and not the polarization state of the light, so only the first parameter S_0 in S_{out} could be measured. Therefore, by rearranging Eq. (4), the polarization measurement equation can be obtained as:

$$I = A \cdot S_{in} \quad (5)$$

where A is the ideal polarization measurement matrix of the system, which is expressed as:

$$A(i,:) = 0.5 \cdot [1, \cos 2\theta_{pi}, \sin 2\theta_{pi}, 0] \quad i = 1,2,3 \quad (6)$$

$$\begin{aligned} A(4,:) = {} & 0.5 \cdot [1, \cos 2\theta_{p4} \cdot (\cos^2 2\theta_r + \cos\delta \cdot \sin^2 2\theta_r) \\ & + \sin 2\theta_{p4} \cdot (\cos 2\theta_r \cdot \sin 2\theta_r - \cos 2\theta_r \cdot \sin 2\theta_r \cdot \cos\delta) \\ & , \sin 2\theta_{p4} \cdot (\cos\delta \cdot \cos^2 2\theta_r + \sin^2 2\theta_r) + \cos 2\theta_{p4} \\ & \cdot (\cos 2\theta_r \cdot \sin 2\theta_r - \cos 2\theta_r \cdot \sin 2\theta_r \cdot \cos\delta), \\ & \cos 2\theta_r \cdot \sin 2\theta_{p4} \cdot \sin\delta - \cos 2\theta_{p4} \cdot \sin 2\theta_r \cdot \sin\delta] \end{aligned} \quad (7)$$

From Eq. (5), the Stokes vector of the incident light is obtained as:

$$S_{in} = \begin{bmatrix} S_0 \\ S_1 \\ S_2 \\ S_3 \end{bmatrix} = B \cdot I \quad (8)$$

where B is the inverse of A. From Eq. (8), the degree of linear polarization ($dolp$) and the polarization angle information Ψ is acquired as:

$$dolp = \frac{\sqrt{S_1^2 + S_2^2}}{S_0}$$
$$\psi = \frac{1}{2}\tan^{-1}\frac{S_2}{S_1} \quad (9)$$

where $0 \le dolp \le 1$.

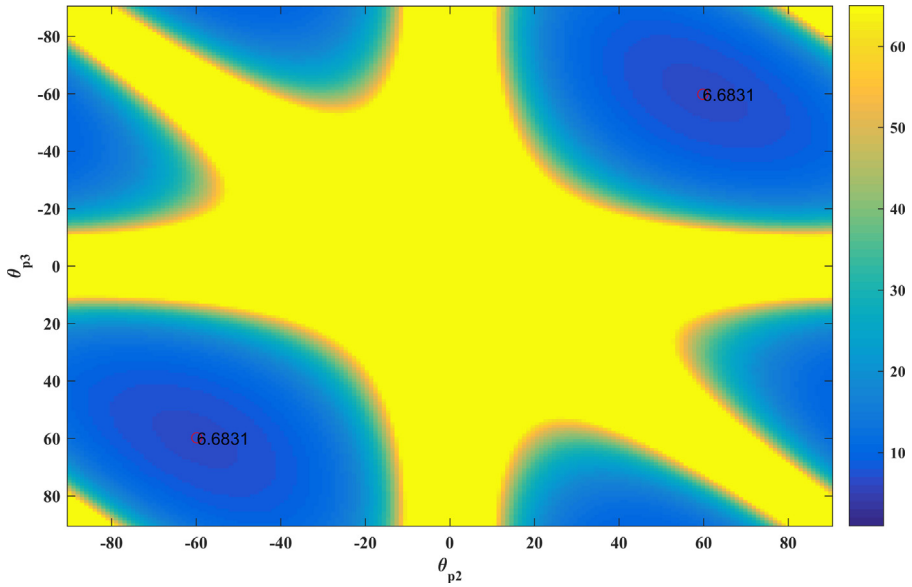

Fig. 3. EWV_{1-3} value of the linear polarization measurement matrix A_{1-3}.

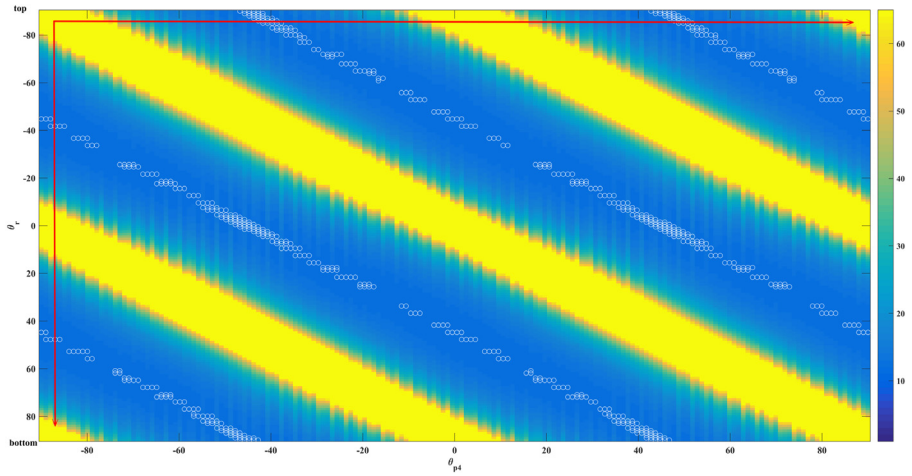

Fig. 4. EWV_A diagram of A.

2.3. Optimization of the polarization measurement matrix

To improve the accuracy of the polarization measurement, random fluctuations in the detection intensity should be effectively suppressed. Different methods are used to optimize the polarization-measurement matrix, including the norm of the matrix [23–27] and equal weight variance (EWV) [28]. Here, we use EWV to optimize the polarization-measurement matrix, which is expressed as follows:

$$EWV = \sum_{j=0}^{3}\sum_{k=0}^{N-1}(A^{+})_{j,k}^{2} = \sum_{j=0}^{R-1}1/\mu_j^2 \tag{10}$$

where A is the measurement matrix of the system, A^{+} is the pseudo inverse matrix of A, N is the number of polarization measurements, R is the rank of A and μ_j is the singular value of A.

The optimization is divided into two steps according to the characteristics of PMS.

Step 1: Optimization of the linear polarization-measurement channel

$$A_{1-3} = \frac{1}{2}\begin{bmatrix} 1, \cos 2\theta_{p1}, \sin 2\theta_{p1} \\ 1, \cos 2\theta_{p2}, \sin 2\theta_{p2} \\ 1, \cos 2\theta_{p3}, \sin 2\theta_{p3} \end{bmatrix} \tag{11}$$

To optimize A_{1-3}, we let $\theta_{p1} = 0°$. EWV_{1-3} of the matrix A_{1-3} is a function of θ_{p2} and θ_{p3}, and EWV_{1-3} with the change in θ_{p2} and θ_{p3}, as shown in Fig. 3. Fig. 3 shows that when the azimuthal angle for the polarizer in the linear polarization-measurement channel is 0°, −60°, and 60°, the value of EWV_{1-3} for A_{1-3} is the smallest, with a minimum value of 6.6831.

Step 2: Optimization of A containing a circularly polarized channel under the premise that the linearly polarized channel azimuth is known.

In the case of θ_{p1}, θ_{p2} and θ_{p3}, A is optimized, i.e., fourth channels θ_{p4} and θ_r are optimized, and EWV_A changes with θ_{p4} and θ_r, as shown in Fig. 4. When the minimum value of EWV_A is 12, we test θ_{p4} and θ_r to find the relationship between the two, as shown in Fig. 4. The red arrow in Fig. 4 indicates the sampling direction. Dots were sampled line by line from the top to the bottom. The white circle represents the minimum value of 12 in Fig. 4. The sampling results are shown in Fig. 5. They satisfy the following relationship:

$$\left|\theta_{p4} - \theta_r\right| = 45° \text{ or } 135° \tag{12}$$

When $|\theta_{p4} - \theta_r| = 45°$ or $135° \pm 1°$, the EWV_A value of the polarization-measurement matrix changes from 12.0000 to 12.0066, which indicates that the system polarization-measurement matrix is insensitive to measurement errors.

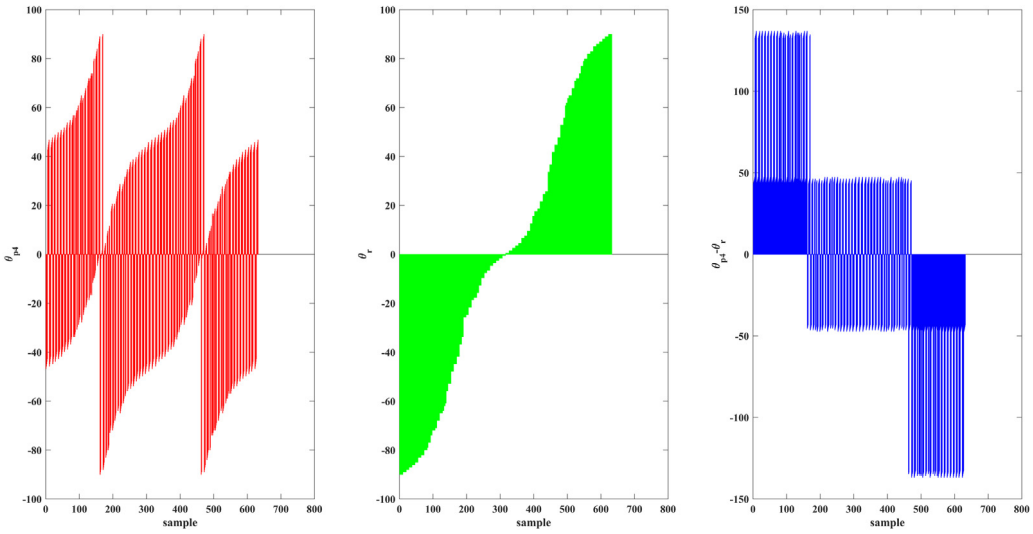

Fig. 5. θ_{p4} and θ_r samples and θ_{p4}–θ_r.

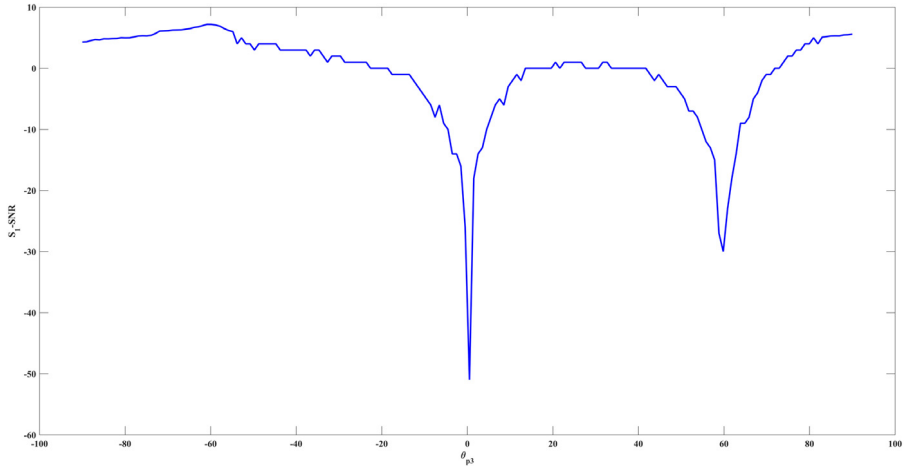

Fig. 6. The curve of the signal-to-noise ratio of S_1 versus θ_{p3}.

2.4. Simulation demonstration of the optimization method

To verify the effectiveness of the optimization obtained in Section 2.3, the ability of the polarization-measurement matrix A to suppress noise should be evaluated. Since we use a cooled HgCdTe detector array with 320 × 256 pixels, Gaussian noise is the main source of noise, and the signal-dependent noise, which is the main noise in quantum-well infrared photodetectors, is neglected.

A Gaussian noise with a mean value of zero and variance of 0.1 is added to the intensity image in Eq. (2). The reconstructed Stokes vector is evaluated for its ability to suppress noise in the linear polarization-measurement channel and circular polarization-measurement channel, where the original Stokes vector satisfies the following relationship [29]:

$$\begin{aligned} S_C &= [1 \quad 1/\sqrt{3} \quad 1/\sqrt{3} \quad 1/\sqrt{3}] \\ S_O &= [0 \quad 0 \quad 0 \quad 0] \end{aligned} \tag{13}$$

where S_C represents the Stokes vector in the central region and S_O represents the Stokes vector in the outer region.

Following the characteristics of optimization for the polarization-measurement matrix, the optimized results in the linear polarization-measurement channel and circular polarization-measurement channel will be evaluated, respectively, as follows:

2.4.1. Linear polarization-measurement channel

The polarization axis direction of the linear polarizer 1, 2 are set as (0°, 60°) relative to the x-axis. When θ_{p3} changes from −90° to 90°, the curve of the signal-to-noise ratio for S_1 and S_2 are shown in Figs. 6 and 7. As seen from Figs. 6 and 7, when θ_{p3} is equal to −60°, the signal-to-noise ratio of S_1 and S_2 are at the maximum value. This is consistent with the optimized result obtained in Section 2.3.

2.4.2. Circular polarization-measurement channel

When the polarization axis direction of the polarizer 1, 2 ,3 and 4 relative to the x-axis is set as (0°, −60°, 60° and 0°), the phase delay of the quarter-wave plate is 90°, and the signal-to-noise ratio of S_3 is a function of θ_r. When θ_r changes from −90° to 90°, the curve of the signal-to-noise ratio for S_3 is shown in Fig. 8. As seen from Fig. 8, when θ_r is equal to 45° or −45°, the signal-to-noise ratio of S_3 is at the maximum value. This is consistent with the optimized result obtained in Section 2.3.

3. Calibration theory of the SMWIFPIS

3.1. The Fourier analysis method of the RRFPSP

Fig. 9 is a schematic diagram of the RRFPSP. The RRFPSP is mainly composed of a rotated quarter-wave plate, a fixed line polarizer, an

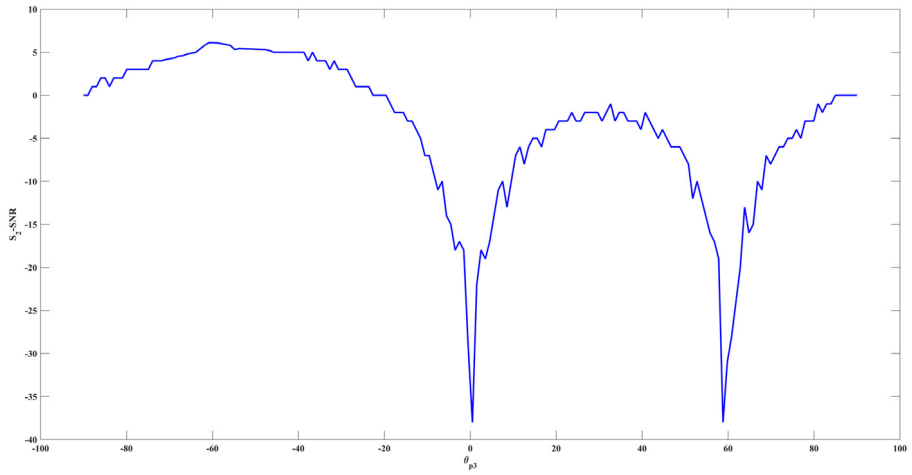

Fig. 7. The curve of the signal-to-noise ratio of S_2 versus θ_{p3}.

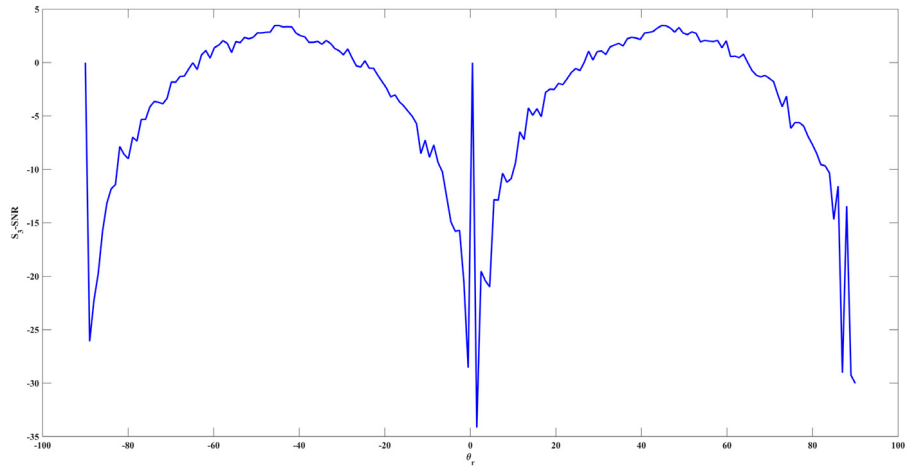

Fig. 8. The curve of the signal-to-noise ratio of S_3 versus θ_r.

imaging optics system and a detector. The polarization axis of the linear polarizer is used as the datum axis, and the fast-axis azimuth angle of the quarter-wave plate is determined by this axis. The light emitted by the target object is modulated by the quarter-wave plate and linear polarizer, and then the image is obtained on the detector through the imaging optics system. The light intensity signal I on the detector can be expressed in Fourier series [30]:

$$I = \frac{a_0}{2} + \frac{1}{2}\sum_{n=1}^{2}\left(a_{2n}\cos 2n\varphi + b_{2n}\sin 2n\varphi\right) \tag{14}$$

where φ is the angle between the fast axis of the wave plate and the polarizer polarization axis, a_0, a_{2n}, b_{2n} are the Fourier coefficient.

The relationship between Stokes parameter S_{in} of incident light and Fourier coefficients by Muller matrix operation can be obtained:

$$\begin{aligned} S_0 &= a_0 - a_4 \\ S_1 &= 2a_4 \\ S_2 &= 2b_4 \\ S_3 &= -b_2 \end{aligned} \tag{15}$$

3.2. Error calibration and compensation principle of the SMWIFPIS

Based on the Fourier analysis method of the RRFPSP and the polarization-measurement structure of the SMWIFPIS, the calibration of SMWIFPIS is divided into the calibration of line polarization measurement channel and circular polarization measuring channel.

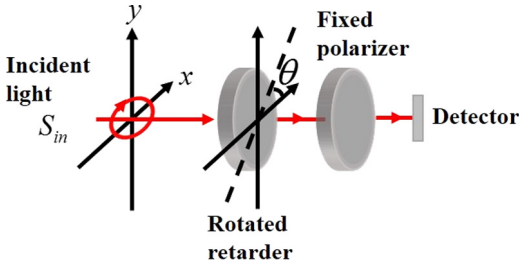

Fig. 9. Schematic diagram of the RRFPSP.

3.2.1. The calibration of the line polarization measurement channel

A standard quarter-wave plate is added to the line polarization measurement channel, which is shown in Fig. 10. The phase delay error of this wave plate is known and the fast axis azimuth angle can be controlled accurately. In each line polarization measurement channel, the polarization axis direction of the linear polarizer in PMS is used as the datum axis, and the fast axis azimuth angle of the standard quarter-wave plates is determined by this axis. Due to the polarization axis with azimuth angle error as the datum axis, this leads to the azimuth error of the linear polarizer being transplanted to the fast axis azimuth angle of the standard quarter-wave plate. Therefore, the azimuth error of the polarizer in the line polarization measurement channel can be

$$M_R = \begin{bmatrix} 1 & 0 & 0 & 0 \\ 0 & \cos^2 2(\varphi+\varepsilon_i) + \sin^2 2(\varphi+\varepsilon_i)\cos(\delta+\sigma_i) & \sin 2(\varphi+\varepsilon_i)\cos 2(\varphi+\varepsilon_i)(1-\cos(\delta+\sigma_i)) & -\sin 2(\varphi+\varepsilon_i)\sin(\delta+\sigma_i) \\ 0 & \sin 2(\varphi+\varepsilon_i)\cos 2(\varphi+\varepsilon_i)(1-\cos(\delta+\sigma_i)) & \sin^2 2(\varphi+\varepsilon_i) + \cos^2 2(\varphi+\varepsilon_i)\cos(\delta+\sigma_i) & \cos 2(\varphi+\varepsilon_i)\sin(\delta+\sigma_i) \\ 0 & \sin 2(\varphi+\varepsilon_i)\sin(\delta+\sigma_i) & -\cos 2(\varphi+\varepsilon_i)\sin(\delta+\sigma_i) & \cos(\delta+\sigma_i) \end{bmatrix} \quad (16)$$

Box II.

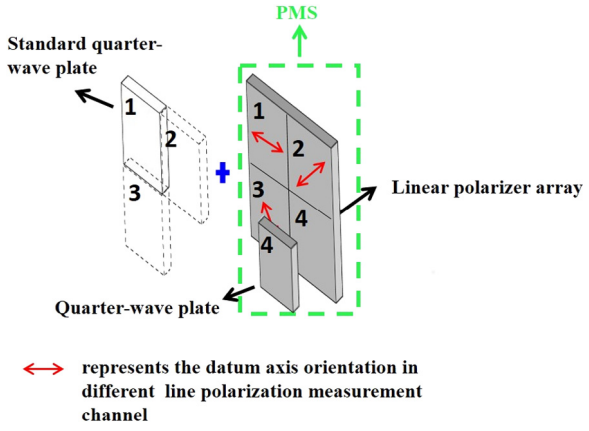

Fig. 10. Schematic diagram of the calibrated structure in the linear polarization measurement channel.

indirectly obtained by measuring the fast axis azimuth error of the standard quarter-wave plate.

It is assumed that the fast axis azimuth error of the standard quarter-wave plate is ε_i and the phase delay error is σ_i, the Muller matrix of the wave plate is given in Box II.

Due to the polarization axis direction of the linear polarizer is used as the datum axis in each polarization measurement channel, so Muller matrix of the linear polarizer is:

$$M_{LP} = \frac{1}{2}\begin{bmatrix} 1 & 1 & 0 & 0 \\ 1 & 1 & 0 & 0 \\ 0 & 0 & 0 & 0 \\ 0 & 0 & 0 & 0 \end{bmatrix} \quad (17)$$

Using small angle approximation (i.e. $\sin\theta = \theta$, $\cos\theta = 1$) and matrix operations, the light intensity expression on the detector can be expressed:

$$\begin{aligned} I = {} & \frac{1}{2}[S_0 + \frac{1}{2}(1-\varepsilon_i)\cdot S_1 + \frac{1}{2}(1+\sigma_i)\cos 4\varepsilon_i \cos 4\varphi \cdot S_1 \\ & -2\varepsilon_i(1+\sigma_i)\cos 2\varepsilon_i \sin 4\varphi \cdot S_1 + \frac{1}{2}(1+\sigma_i)\cos 4\varepsilon_i \sin 4\varphi \cdot S_2 \\ & +2\varepsilon_i(1+\sigma_i)\cos 2\varepsilon_i \cos 4\varphi \cdot S_2 - \cos 2\varepsilon_i \sin 4\varphi \cdot S_3 - 2\varepsilon_i \cos 2\varphi \cdot S_3] \end{aligned} \quad (18)$$

where i represent the ith polarization measurement channel.

Comparing Eqs. (18) and (14), the Fourier coefficients in (14) are obtained:

$$\begin{aligned} a_0 &= S_0 + \frac{1}{2}(1-\sigma_i)\cdot S_1 \\ a_2 &= -2\varepsilon_i \cdot S_3 \\ a_4 &= \frac{1}{2}(1+\sigma_i)\cos 4\varepsilon_i \cdot S_1 + 2\varepsilon_i(1+\sigma_i)\cos 2\varepsilon_i \cdot S_2 \\ b_2 &= -\cos 2\varepsilon_i \cdot S_3 \\ b_4 &= \frac{1}{2}(1+\sigma_i)\cos 4\varepsilon_i \cdot S_2 - 2\varepsilon_i(1+\sigma_i)\cos 2\varepsilon_i \cdot S_1 \end{aligned} \quad (19)$$

According to Eq. (19), the Stokes vector of the incident light can be obtained as follows:

$$\begin{aligned} S_0 &= a_0 - \gamma S_1 \\ S_1 &= \frac{\alpha a_4 - \beta b_4}{\alpha^2+\beta^2} \\ S_2 &= \frac{\alpha b_4 + \beta a_4}{\alpha^2+\beta^2} \\ S_3 &= -\frac{b_2}{\cos 2\varepsilon_i} \end{aligned} \quad (20)$$

where

$$\begin{aligned} \alpha &= \frac{1}{2}(1+\sigma_i)\cos 4\varepsilon_i \\ \beta &= 2\varepsilon_i(1+\sigma_i)\cos 2\varepsilon_i \\ \gamma &= \frac{1}{2}(1-\sigma_i) \end{aligned} \quad (21)$$

So the relationship between the Stocks vector of the incident light and the azimuth error and phase delay error of the wave plate is obtained.

In each line polarization measurement channel, the linear polarized light parallel to the polarization axis of the polarizer is used as the incident light. Because the polarization axis with azimuth angle error is used as the datum axis, there is a ε_i angle deviation between the actual linear polarized light and the ideal linear polarized light. The actual linear polarized light S_{in} can be expressed:

$$S_{in} = \begin{bmatrix} 1 \\ \cos(2\varepsilon_i) \\ \sin(2\varepsilon_i) \\ 0 \end{bmatrix} \quad (22)$$

The Eq. (22) is brought into Eq. (19), the Fourier coefficients are obtained:

$$\begin{aligned} a_0 &= 1 + \frac{1}{2}(1-\sigma_i)\cdot\cos 2\varepsilon_i \\ a_2 &= 0 \\ a_4 &= \frac{1}{2}(1+\sigma_i)\cos 4\varepsilon_i \cdot \cos 2\varepsilon_i + 2\varepsilon_i(1+\sigma_i)\cos 2\varepsilon_i \cdot \sin 2\varepsilon_i \\ b_2 &= 0 \\ b_4 &= \frac{1}{2}(1+\sigma_i)\cos 4\varepsilon_i \cdot \sin 2\varepsilon_i - 2\varepsilon_i(1+\sigma_i)\cos 2\varepsilon_i \cdot \cos 2\varepsilon_i \end{aligned} \quad (23)$$

In order to guarantee the uniqueness of the solution and minimize the effect of the small angle approximation on the calibration result, just make the $\cos 2\varepsilon_i = 1$, $(\varepsilon_i)^2 = 0$. The two error parameters can be obtained from Eq. (23):

$$\begin{aligned} \frac{\cos 4\varepsilon_i}{\varepsilon_i \cdot \cos 4\varepsilon_i - 4\varepsilon_i} &= \frac{a_4}{b_4} \\ \sigma_i &= 3 - 2a_0 \end{aligned} \quad (24)$$

Therefore, we use the linear polarized light which is parallel to the polarization axis of the polarizer as the measuring object. By rotating standard wave-plate method and performing the Fourier analysis of the measured light intensity, the azimuth angle error and the phase delay error of the standard quarter-wave plate are obtained from Eq. (24). The azimuth error of the polarizer in the line polarization measurement channel can be indirectly known from ε_i.

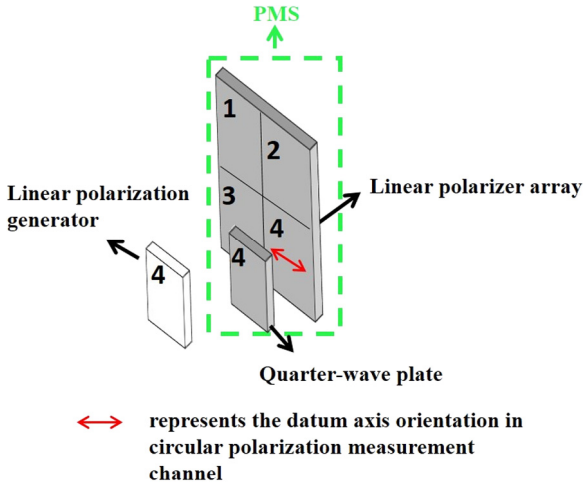

Fig. 11. Schematic diagram of the calibrated structure in the circular polarization measurement channel.

3.2.2. The calibration of the circular polarization measurement channel

In the circular polarization measurement channel, the polarization axis direction of the linear polarizer in PMS is also used as the datum axis, and the fast axis azimuth angle of the quarter-wave plates is determined by this axis. A linear polarization generator is added to the circular polarization measurement channel, which can produce linear polarized light in different polarization directions ϕ to incident this channel. The calibrated structure is illustrated as shown in Fig. 11.

The linear polarized light generated by the linear polarization generator can be expressed:

$$S_{in} = \begin{bmatrix} 1 \\ \cos 2(\varepsilon_i + \phi) \\ \sin 2(\varepsilon_i + \phi) \\ 0 \end{bmatrix} \tag{25}$$

We perform the Fourier analysis of the measured light intensity, then the azimuth angle error and the phase delay error of the quarter-wave plate in the circular polarization measurement channel are obtained from Eq. (19).

By calibrating the error of the line polarization channel and the circular polarization channel, the polarization measurement matrix A is modified and the measurement accuracy is improved.

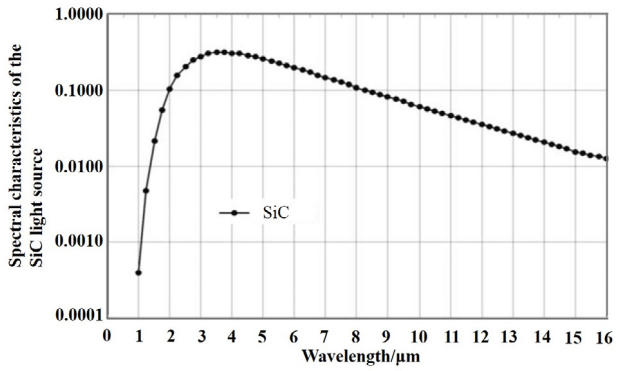

Fig. 13. The spectral characteristics of the SiC light source.

4. Experiment and result analysis

4.1. Calibration device

A calibration device of the SMWIFPIS is shown in Fig. 12, which is mainly composed of a SiC infrared light source, a medium-wave infrared collimating system, a linear polarizer, a standard quarter-wave plate, a SMWIFPIS and a detector. The combination of the light source, collimating system and linear polarizer is used to generate the linear polarized light with different polarization direction, which is called linear polarization state generator (LPSG). The standard quarter-wave plate is added to the line polarization measurement channel, which is used to indirectly measure the azimuthal angle error of the linear polarization element in the PMS due to the misalignment.

The spectral range of the infrared SiC light source is 1–16 μm, the spectral characteristics of the SiC infrared light source is shown in Fig. 13. The working band range of the collimating system is 3–5 μm, with a design wavelength of 4 μm. The combination of the light source and collimating system is used to generate the medium-wave infrared light, whose wavelength range is 3–5 μm. The detector is a cooled HgCdTe detector array with 320 × 256 pixels, whose pixel size is 30 μm. Its response band range is 3.7–4.8 μm and the central wavelength is 4 μm. The material used for the retarder is magnesium fluoride, which has a phase delay and phase delay accuracy of 270° and $\lambda/300$, respectively. The diameter and extinction ratio of the silicon wire grid polarizer is 25 mm and more than 1000:1, respectively. The linear polarizer in LPSG and standard quarter-wave plate are all fixed on the precision rotary table with a rotational accuracy of 5′.

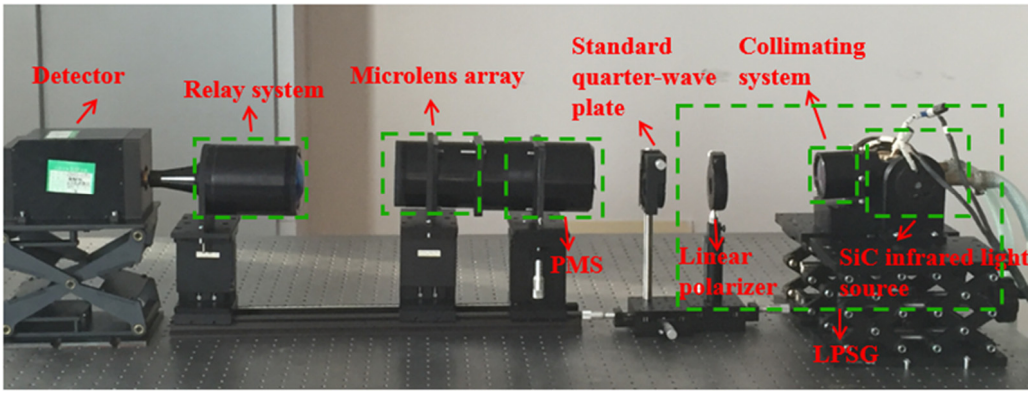

Fig. 12. The calibration device of the SMWIFPIS.

Table 1
Measurement results in channel 1.

	Value	Error/%
S_1	1.0386	3.86%
S_2	−0.0383	−3.83%
S_3	−0.0035	−0.35%
ε_2	−1.0952°	–
σ_2	1.2291°	–

Table 2
Measurement results in channel 2.

	Value	Error/%
S_1	0.9798	−2.02%
S_2	0.0182	1.82%
S_3	0.0034	0.34%
ε_1	0.5210°	–
σ_1	1.2271°	–

Table 3
Measurement results in channel 3.

	Value	Error/%
S_1	0.9636	−3.64%
S_2	−0.0208	−2.08%
S_3	0.0049	0.49%
ε_3	−0.5963°	–
σ_3	1.2301°	–

Table 4
The azimuth and phase delay error of the quarter-wave plate in channel 4.

Parameter	Value
ε_4	−1.0341°
σ_4	1.3024°

4.2. Calibration process and results

The line polarization channel calibration method: the polarization axis direction of the linear polarizer in PMS is used as the datum axis, which determine the fast axis azimuth angle of the standard quarter-wave plate and polarization axis direction of the linear polarizer in LPSG. The linear polarized light parallel to the datum axis is generated by rotating the polarizer in LPSG. In the measurement process, the fast axis of the standard quarter-wave plate relative to the datum axis rotates 10°, 20°, 30°, 40°, 50° and 60°. Some images are collected at each rotation angle. The azimuth and phase delay error of the standard quarter-wave plate can be obtained by data processing and numerical calculation. The data measured in the experiment in the linear polarization measurement channel are as follows.

The circular polarization channel calibration method: the standard quarter-wave plate is removed when the calibration is done in the circular polarization channel. The polarization axis direction of the linear polarizer 4 in PMS is used as the datum axis, which determine the fast axis azimuth angle of the quarter-wave plate in PMS and polarization axis direction of the linear polarizer in LPSG. In the measurement process, polarization axis direction of the linear polarizer in LPSG relative to the datum axis rotates 0°, 10°, 20°, 30°, 40° and 50°. Some images are collected at each rotation angle. The azimuth and phase delay error of the quarter-wave plate in PMS can be obtained by data processing and numerical calculation. The data are as follows

From Tables 1 to 4, we can get polarization axis direction errors of the polarizers in linear polarization measurement channel are −1.0952°, 0.5210°, −0.5963°, respectively. The azimuth and phase delay error of the quarter-wave plate in circular polarization measurement channel are −1.0341° and 1.3024°. The actual polarization measurement matrix A_A after calibration is:

$$A_a = \begin{bmatrix} 0.5 & 0.4996 & -0.0191 & 0 \\ 0.5 & -0.2421 & -0.4375 & 0 \\ 0.5 & -0.2409 & 0.4381 & 0 \\ 0.5 & 0.0120 & 0.0176 & 0.4995 \end{bmatrix} \tag{26}$$

The ideal polarization measurement matrix A_i is:

$$A_i = \begin{bmatrix} 0.5 & 0.5 & 0 & 0 \\ 0.5 & -0.25 & -0.433 & 0 \\ 0.5 & -0.25 & 0.433 & 0 \\ 0.5 & 0 & 0 & 0.5 \end{bmatrix} \tag{27}$$

A verification experiment was carried out in order to verify the correctness of calibration. The horizontal x axis is used as the datum axis and the azimuth angle of the polarization element in PMS is determined by this axis. The linear polarized light is generated as a reference light by LPSG, whose polarization direction is parallel to x axis. The measured results before and after the calibration are as follows.

Table 5
Measurement results before and after the calibration.

	Before calibration		After calibration	
	Value	Error/%	Value	Error/%
S_1	0.9861	−1.39%	0.9967	−0.32%
S_2	0.0047	0.47%	0.0040	0.40%
S_3	0.0341	3.41%	0.0171	1.83%

It can be seen from Table 5 that the deviation between S_1, S_2, S_3 and theoretical value is −1.39%, 0.47%, 3.41% before error compensation. After the error compensation, the deviation of the Stokes vector from the theoretical value is reduced to −0.32%, 0.40% and 1.83%, respectively.

The experimental results show that the calibration theory of SMWIFPIS is correct and the measurement accuracy is obviously improved.

4.3. A test experiment

In order to verify the performance of the SMWIFPIS, a test experiment is carried out. The test device of the SMWIFPIS is the same as the calibration device, which is shown in Fig. 12.

The test process is as follows: The horizontal x axis is used as the datum axis. The polarization axis direction of the linear polarizer in LPSG relative to x axis is 0°, therefore the Stokes vector $[1\ 1\ 0\ 0]^{\mathrm{T}}$ is generated by LPSG. When the incident light passes through the standard quarter-wave plate, the Stokes vector of the outgoing can be obtained as:

$$S_{oR} = M_{SR} \cdot \begin{bmatrix} 1 \\ 1 \\ 0 \\ 0 \end{bmatrix} = \begin{bmatrix} 1 \\ \cos^2 2\theta_{SR} + \sin^2 2\theta_{SR} \cos\delta \\ \sin 2\theta_{SR} \cos 2\theta_{SR} (1 - \cos\delta) \\ \sin 2\theta_{SR} \sin\delta \end{bmatrix} \tag{28}$$

where M_{SR} is the Muller matrix of the standard quarter-wave plate, θ_{SR} is the angle of the fast axis of the standard quarter wave plate relative to x axis.

By rotating the standard quarter-wave plate from −90° to 90°, different polarization states are generated to incident on SMWIFPIS, which is shown in Fig. 14. The real lines represent the theoretical data. The sample data points represent the normalized experimental data measured by SMWIFPIS, the rotated interval is 10°.

As we can see from Fig. 14, the incident light in different polarization states measured by the SMWIFPIS is accurate. The average measurement errors of S_1, S_2, and S_3 were 0.78%, 0.94%, and 1.74%, respectively.

In addition, there are some measurement errors after calibration. This is mainly due to the changes (such as temperature, humidity, vibration) in the experimental environment as well as the accuracy of the rotary table and other factors, which must influence measurement results in the system to a certain extent.

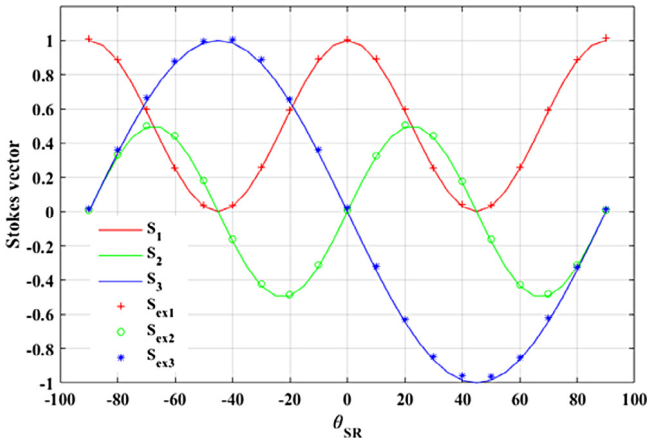

Fig. 14. Theory and normalized experimental data.

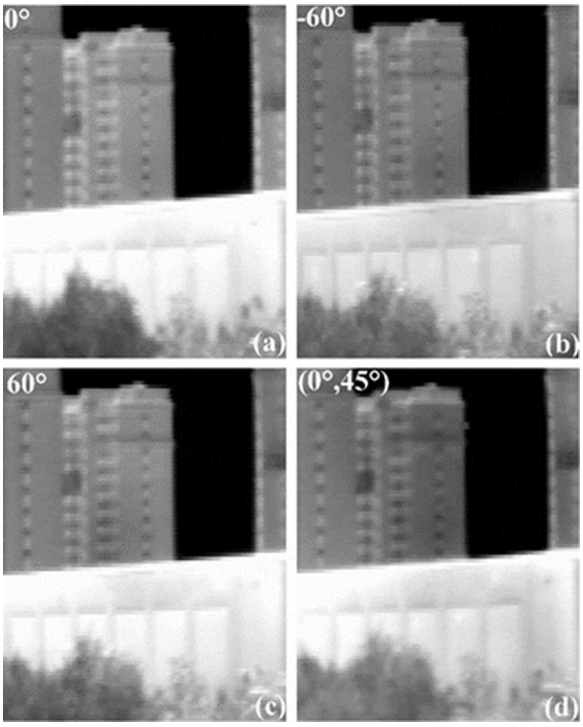

Fig. 15. Intensity image on the four quadrants of the single detector.

4.4. Preliminary experimental results of the SMWIFPIS

After the polarization calibration, a polarization imaging experiment utilizing the SMWIFPIS was carried out. The detected wavelength range is 3.7–4.8 μm. The temperature of the environment was 20 °C.

To obtain accurate polarization information, the individual images at the four divisions of a single detector are pre-processed by a scale invariant feature transform algorithm to calculate overlapping regions among the individual images. A few buildings were identified by extraction from overlapping regions at the four divisions of the detector, as shown in Fig. 15.

The Stokes-vector, line-polarization degree, and polarization-angle images of the target scene are calculated using Eqs. (8)–(9), as shown in Figs. 16 and 17.

It can be seen from Figs. 15 to 16 that the intensity image can show the rough outline, and the details of the image are not clear, such as the layered structure of the building and the outline of the window. However, these details are clear in the Stokes vector images. It can be seen from Fig. 17 that the direction information of the target scene is effectively extracted in the linear polarization image and the polarization angle image. The layered structure of the building and the outline of the window are clearer. This further shows that the polarization calibration is accurate.

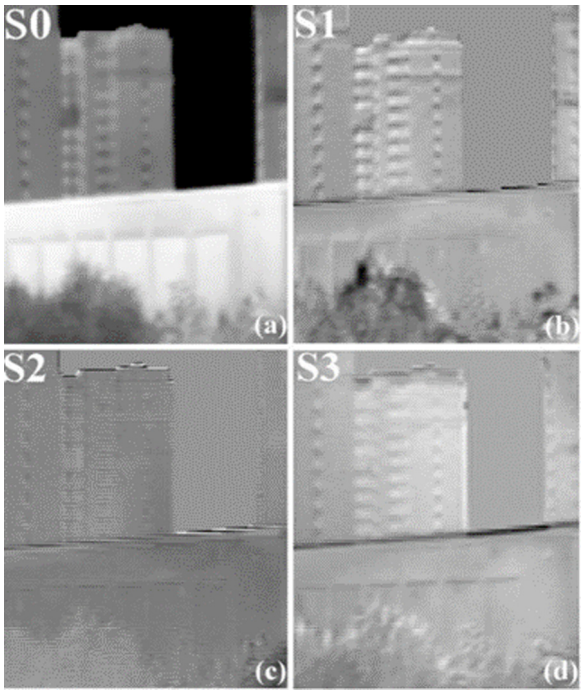

Fig. 16. Stokes vector images.

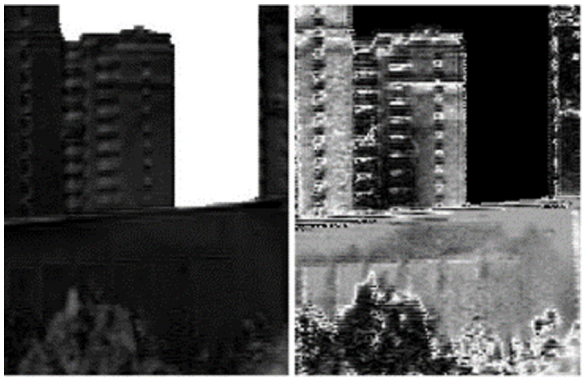

Fig. 17. Degree of linear polarization image (left) and polarization angle image (right).

5. Conclusions

A snapshot, mid-wave infrared full-polarization-imaging system is presented. By using the optimization method of equal weight variance, the polarization axis direction of the polarizer in different channels was optimized to suppress the effect of detector intensity fluctuations on polarization measurement. The optimization results show that when the polarization direction of the polarizer in the linear polarization measurement channel relative to the x-axis is 0°, −60°, 60°, and the angle between the fast axis of wave plate and the polarizer polarization axis in the circular polarization measurement channel is 45° or 135°, the signal-to-noise ratio of the reconstructed Stokes vector is highest. The

calibration theory of the system is deduced based on Fourier analysis method of a rotatable retarder fixed polarizer Stokes polarimeter. The experimental results show that the calibration theory of SMWIFPIS is correct and the measurement accuracy is obviously improved. The incident light in different polarization states measured by the SMWIFPIS is accurate. This study is instructive for an accurate measurement of polarization information of polarization-imaging systems and polarization-interference-imaging systems.

Acknowledgments

We gratefully acknowledge the National Nature Science Foundation of China (61376122, 61627819, 61575193, 6173000222, 6172780148); the Science and Technology Development Plan of Jilin Province (20170204077GX, 20150204072GX, 20150520101JH, 20150101049JC); and the State Key Laboratory of Applied Optics Independent Fund and Youth Innovation promotion Association CAS (2014193).

References

[1] K.M. Twietmeyer, R.A. Chipman, A.E. Elsner, Y. Zhao, D. VanNasdale, Mueller matrix retinal imager with optimized polarization conditions, Opt. Express 16 (26) (2008) 21339–21354.
[2] S. Alali, A. Vitkin, Polarized light imaging in biomedicine: emerging Mueller matrix methodologies for bulk tissue assessment, J. Biomed. Opt. 20 (6) (2015) 0611041–0611049.
[3] F.Y. Yue, C.M. Zhang, X.F. Zang, D. Wen, B.D. Gerardot, S. Zhuang, X.Z. Cheng, High-resolution grayscale image hidden in a laser beam, Light:Sci. Appl. 7 (2018) 17129.
[4] Q.Z. Cao, J. Zhang, E. Dehoog, Y. Lu, B.Q. Hu, W.G. Li, J.Y. Li, D.X. Fan, T. Deng, Y. Yan, Static subminiature snapshot imaging polarimeter using spatial modulation, Acta Phys. Sin. 65 (5) (2016) 050702-1-05070-10.
[5] L. Li, T. Li, X.M. Tang, S.M. Wang, Q.J. Wang, S.N. Zhu, Plasmonic polarization generator in well-routed beaming, Light:Sci. Appl. 4 (2015) e330.
[6] J.S. Tyo, D.L. Goldstein, B.C. David, J.A. Shaw, Review of passive imaging polarimetry for remote sensing applications, Appl. Opt. 45 (22) (2006) 5453–5469.
[7] T.K. Mu, C.M. Zhang, C.L. Jia, W.Y. Ren, Static hyperspectral imaging polarimeter for full linear stokes parameters, Opt. Express 20 (16) (2012) 18194–18201.
[8] J.S. Tyo, M.P. Rowe, E.N. Pugh, N. Engheta, Target detection in optically scattering media by polarization difference imaging, Appl. Opt. 35 (11) (1996) 1855–1870.
[9] E. Maguid, I. Yulevich, M. Yannai, V. Kleiner, M.L. Brongersma, E. Hasman, Multifunctional interleaved geometric-phase dielectric metasurfaces, Light:Sci. Appl. 6 (2017) e17027.
[10] R.M. Azzam, Arrangement of four photodetectors for measuring the state of polarization of light, Opt. Lett. 10 (7) (1985) 309–311.
[11] A.G. Andreou, Z.K. Kalayjian, Polarization imaging: principles and integrated polarimeters, Sensors J. IEEE 2 (6) (2002) 566–576.
[12] T.K. Mu, C.M. Zhang, Q. Li, R. Liang, Error analysis of single-snapshot full-Stokes division-of-aperture imaging polarimeters, Opt. Express 23 (8) (2015) 10822–10835.
[13] Y. Zhang, H. Zhao, N. Li, Polarization calibration with large apertures in full field of view for a full Stokes imaging polarimeter based on liquid-crystal variable retarders, Appl. Opt. 52 (6) (2013) 1284–1292.
[14] T.K. Mu, C.M. Zhang, W. Ren, C. Jia, Static polarization difference interference imaging spectrometer, Acta Phys. Sin. 37 (17) (2014) 3507–3509.
[15] E.L. Dereniak, M.J. Escuti, N. Hagen, E. Dereniak, K. Oka, Snapshot imaging Mueller matrix polarimeter using polarization gratings, Opt. Lett. 37 (8) (2012) 1367–1369.
[16] T.H. Tsai, D.J. Brady, Coded aperture snapshot spectral polarization imaging, Appl. Opt. 52 (10) (2013) 2153–2161.
[17] X. .Jian, C. Zhang, Y. Sun, L. Wu, Novel polarization interference imaging spectrometer with adjustable lateral displacement Savart polariscope, Acta Opt. Sin. 27 (4) (2007) 643–646.
[18] D. Colas, L. Dominici, Polarization shaping of Poincaré beams by polariton oscillations, Light:Sci. Appl. 4 (2015) E350.
[19] R.M. Azzam, E. Masetti, I. Elminyawi, F.G. Grosz, Construction, calibration, and testing of a four detector photopolarimeter, Rev. Sci. Instrum. 59 (1) (1988) 84–88.
[20] R. Azzam, Accurate calibration of the four-detector photopolarimeter with imperfect polarizing optical elements, J. Opt. Soc. Am. A 6 (6) (1989) 1513–1521.
[21] R.M. Azzam, Stokes-vector and mueller-matrix polarimetry, J. Opt. Soc. Amer. A 33 (77) (2016) 1396–1408.
[22] S.A. Hall, M.A. Hoyle, J.S. Post, D.K. Hore, Combined Stokes vector and Mueller matrix polarimetry for materials characterization, Anal. Chem. 85 (15) (2013) 7613–7619.
[23] A. Ambirajan, D.C. Look, Optimum angles for a polarimeter: part I, Opt. Express 34 (34) (1995) 1651–1655.
[24] A. Peinado, A. Lizana, J. Vidal, C. Lemmi, J. Campos, Optimization and performance criteria of a Stokes polarimeter based on two variable retarders, Opt. Express 18 (10) (2010) 9815–9830.
[25] J.S. Tyo, Z.P. Wang, S.J. Johnson, B.G. Hoover, Design and optimization of partial Mueller matrix polarimeters, Appl. Opt. 49 (12) (2010) 2326–2333.
[26] P. Lemaillet, B.L. Jeune, S. Rivet, Optimization of a snapshot Mueller matrix polarimeter, Opt. Lett. 33 (2) (2008) 144–166.
[27] E.L. Dereniak, H. Luo, K. Oka, N. Hagen, T. Tkaczyk, Modeling and optimization for a prismatic snapshot imaging polarimeter, Appl. Opt. 45 (33) (2006) 8400–8409.
[28] D.S. Sabatke, M.R. Descour, E.L. Dereniak, W.C. Sweatt, S.A. Kemme, G.S. Phipps, Optimization of retardance for a complete Stokes polarimeter, Opt. Lett. 25 (11) (2000) 802–804.
[29] F. Goudail, Noise minimization and equalization for Stokes polarimeters in the presence of signal-dependent Poisson shot noise, Opt. Lett. 34 (5) (2009) 647–649.
[30] D. Goldstein, Polarized Light, third ed., Taylor & Francis Inc., Florida, USA, 2010, pp. 105–133.